



# Oscillatory hydraulic testing as a strategy for NAPL source zone monitoring: Laboratory experiments



YaoQuan Zhou \*, Michael Cardiff

Department of Geoscience, University of Wisconsin-Madison, Madison, WI, USA

## ARTICLE INFO

### Article history:

Received 15 August 2016

Received in revised form 8 February 2017

Accepted 17 March 2017

Available online 21 March 2017

### Keywords:

Oscillatory hydraulic tomography

NAPL characterization

Inverse modeling

Laboratory sandbox

## ABSTRACT

Non-aqueous phase liquids (NAPLs) have a complex mode of transport in heterogeneous aquifers, which can result in pools and lenses of NAPLs (the “source zone”) that are difficult to detect and can cause long-term contamination via slow dissolution into groundwater (the “dissolved plume”). Characterizing the extent and evolution of NAPL contamination within the source zone is a useful strategy for designing and adapting appropriate remedial actions at many contaminated sites. As a NAPL flows into a given aquifer volume, the effective hydraulic conductivity ( $K$ ) and specific storage ( $S_s$ ) of the volume changes associated with the viscosity and compressibility of the impinging fluid, meaning that NAPL movement may be detectable with hydraulic testing. Recently, the use of oscillatory pumping tests – in which sinusoidal pumping variations are implemented and oscillatory pressure changes are detected at monitoring locations – has been suggested as a low-impact hydraulic testing strategy for characterizing aquifer properties (Cardiff et al., 2013; Zhou et al., 2016). Here, we investigate this strategy in an experimental laboratory sandbox where dyed vegetable oil is injected and allowed to migrate as a NAPL. Initial qualitative analyses demonstrate that measurable changes in pressure signal amplitude and phase provide clear evidence for NAPL plume emplacement and migration. Using the approach developed in Zhou et al. (2016), we then apply tomographic analyses to estimate the location of effective  $K$  changes (representing fluid changes) and their movement throughout time. This approach provides a method for monitoring ongoing NAPL movement without net extraction or injection of fluid, making it advantageous in field remediation applications.

© 2017 Elsevier B.V. All rights reserved.

## 1. Introduction

Remediation of aquifers contaminated by non-aqueous phase liquids (NAPLs) has been a major technical, economical and environmental challenge for decades. NAPLs such as chlorinated solvents (e.g., trichloroethylene (TCE) and tetrachloroethylene (PCE)), creosote, coal tar, and petroleum chemicals (such as benzene, toluene, xylene, and benzene derivatives) are extensively used in industrial and petroleum processes, and their release into aquifers has contributed to significant sources of groundwater contamination worldwide (Mayer and Hassanizadeh, 2005). The migration of NAPL also presents a complex multiphase flow problem. Over the past two decades, numerous studies have been dedicated to improving the understanding of the mechanisms governing NAPL migration and the evolution of NAPL distributions at contaminated sites. For example, Kueper et al. (1993) and Brewster et al. (1995) performed controlled spill field experiments to study the factors that affect NAPL migration. These studies demonstrated that NAPL distributions are governed by the physical properties of

NAPL (density, viscosity, pressure/saturation curves and saturation/relative permeability relationships) as well as by the heterogeneity in intrinsic aquifer parameters (permeability and storage coefficients). This dependence on many different physical factors ultimately makes the prediction of NAPL distribution and migration following a spill quite difficult, and multiple types of characterization may be necessary in order to effectively predict or monitor NAPL movement.

Characterization of existing NAPL source zones has been performed using a variety of methods. Coring or direct-push sampling can provide direct, localized measurements of aquifer properties and NAPL saturations (e.g., Parker et al., 2003; Parker et al., 2004; Siegrist et al., 2006; Parker et al., 2008). Tracer tests using non-reactive tracers can help to better constrain the permeability, porosity, and dispersivities within an aquifer source zone, while other tailored tracers – using specialized chemicals that are sensitive to NAPL concentration or interfacial area – can help to constrain NAPL distributions (e.g., Annable et al., 1998; Rao et al., 2000). In particular, partitioning tracer tests have shown promise, which are sensitive to encountered NAPL distributions as the tracer passes (e.g., Jin et al., 1995; Annable et al., 1998; Dwarakanath et al., 1999), which may be analyzed tomographically to discern spatial variability in NAPL saturations (e.g., Yeh and Zhu, 2007; Illman et al., 2010). Geophysical methods that are sensitive to fluid properties, such

\* Corresponding author at: Department of Geoscience, University of Wisconsin-Madison, Madison, WI 53706, USA.

E-mail address: [zhou86@wisc.edu](mailto:zhou86@wisc.edu) (Y. Zhou).

as ground penetrating radar (GPR), electrical resistivity tomography (ERT) or induced polarization methods (IP), are especially well-tailored for monitoring changes in aquifer properties over time (e.g., Brewster et al., 1995; Hulihan et al., 2005; Chambers et al., 2010; Revil et al., 2011; Orozco et al., 2012; Babcock and Bradford, 2015). Finally, detailed hydraulic testing (Hochstetler et al., 2015) may be used to better understand heterogeneity in aquifer flow parameters (i.e., hydraulic conductivity,  $K$ ) including the connectivity of high- and low- $K$  zones.

The strong dependence of contaminant transport on aquifer hydraulic conductivity has led to the development of hydraulic tomography (HT), in which a series of pumping tests are performed and head changes are used to tomographically invert for aquifer heterogeneity (Gottlieb and Dietrich, 1995; Yeh and Liu, 2000). Hydraulic tomography has been tested through many numerical, laboratory, and field-scale studies (for a recent summary, see Cardiff and Barrash, 2011) and has been demonstrated as a benefit for contaminated sites through both laboratory studies (Illman et al., 2010) and recent field-scale contaminated site experimentation (Hochstetler et al., 2015). However, the use of pumping tests at contaminated sites can incur substantial costs due to contaminated water treatment requirements. Similarly, injection or extraction pumping tests may have the unintended impact of mobilizing existing contamination. Indeed, approaches to aquifer characterization that do not require significant pumping, such as core sample characterization or direct push methods (e.g., Dietrich et al., 2008; Liu et al., 2009; Dogan et al., 2011) are often viewed more favorably at contaminated sites. That said, these methods are less sensitive to the connectivity of  $K$  structures between sampling points, which are important in controlling flow pathways.

Recently, Cardiff et al. (2013) suggested the use of oscillatory pumping as a less invasive strategy for HT-based aquifer characterization, naming the strategy oscillatory hydraulic tomography (OHT). In this strategy, sinusoidal flowrate changes at a pumping well are used as the stimulation, and the measured head changes at observation wells are used to tomographically infer both aquifer hydraulic conductivity ( $K$ ) and specific storage ( $S_s$ ) variability. As discussed in earlier works, OHT testing using oscillatory pumping tests can be performed in ways that do not require mass extraction – such as by using pistons or pneumatic pressure variations (see, e.g., Cardiff and Barrash, 2015). This approach presents an advantage over traditional pumping tests at sites where contaminated water is present, in that no extraction of water necessarily takes place, and thus treatment costs may be reduced during characterization. In this work, we investigate OHT for monitoring and characterizing NAPL source zones by imaging and detecting changes in these effective aquifer properties. When multiple fluids are present in an aquifer, the effective hydraulic conductivity depends on the soil grain size, the structure of the soil matrix, the fluid phases present, the interfacial tension between phases, and the relative saturation of each fluid phase. Considering a matrix with a single fluid, the movement of the fluid is controlled by the kinematic viscosity  $\nu$  [m<sup>2</sup>/s], the ratio of the dynamic viscosity of the fluid to its density. For a subsurface system saturated with a single fluid phase, the effective hydraulic conductivity,  $K$  [m/s], can be expressed as (Bear, 1972):

$$K = \frac{\kappa g}{\nu} \quad (1)$$

where  $\kappa$  [m<sup>2</sup>], the intrinsic permeability, depends only on the arrangement of pore spaces in the porous media. When NAPL fully infiltrates a given aquifer volume, the fluid kinematic viscosity that determines an “effective” local  $K$  change correspondingly. Therefore, if imaged through HT, areas invaded by NAPL should present a different  $K$  value over time associated with multi-phase fluid movements. In a similar fashion, portions of an aquifer experiencing multiphase flow can experience reduced effective  $K$  locally due to factors such as pore throat blockage. In this work, we test the ability of OHT – using no net extraction or injection – to image effective aquifer  $K$  and  $S_s$  changes in a

laboratory sandbox during infiltration of a high-viscosity LNAPL (dyed vegetable oil). By performing OHT testing at several stages throughout NAPL movement, we are able to monitor NAPL source zone migration throughout time.

It should be noted that while we present results showing the ability of OHT to monitor NAPL distribution changes over time due to natural buoyant movement, OHT could also be applied in other scenarios. For example, by performing OHT characterization of a contaminated site both before and after remediation, changes in effective  $K$  may help to provide verification that remediation has removed NAPL in target areas.

## 2. Methods

### 2.1. Experimental sandbox setup

The experiments carried out in this work utilized the laboratory sandbox described previously in Zhou et al. (2016), though we review some of the key experimental parameters here. The internal dimensions of the sandbox used here are 150 cm in length, 75 cm in height, with a thickness of 10 cm. The sandbox is constructed of 2.5 cm thick Plexiglas (Midland Plastics), bonded by a mixture of Plexiglas and chloroform. When packed with sand, the height of the sand in the tank is 65 cm. The sandbox contains water reservoirs, maintained at a constant water level, on the left and right ends of the domain. After packing with sand, the top is sealed with bentonite clay in order to create a confined aquifer system. To allow instrumentation, the front side of the sandbox contains ports of 6.35 mm diameter at 25 equally spaced locations. In this work, 10 ports were used as observation locations while 5 other ports were available as pumping locations (Fig. 1). Fiber optic pressure transducers (FISO Technologies, Quebec, Canada, <http://www.fiso.com/>), with a sampling frequency of 125 Hz, are used to detect pressure variations at the observation locations. To maintain compression and vertical stability of the sandbox, we clamped Unistrut metal support beams at the front and back of the sandbox.

In packing the sandbox for the experimentation in this work, two types of materials were used: silt, with a low hydraulic conductivity estimated at  $4 \times 10^{-8}$  m/s (ASTM reference soil, Vicksburg Silt), and commercial sand, with an estimated hydraulic conductivity of  $4 \times 10^{-4}$  m/s (Unimin Silica Sand, 40/30), with both materials' properties measured through careful permeameter testing. For these experiments, the sandbox was packed according to the diagram shown in Fig. 1. Similar to earlier HT sandbox experiments by Illman et al. (2010), the packed porous media has the following properties: 1) a simplified heterogeneity pattern with sufficient  $K$  contrast to allow OHT to image the various  $K$  zones; and 2) a low  $K$  zone that will allow NAPL to pool on this layer. Before initiation of the NAPL injection, the sandbox is initially fully saturated with tap water.

### 2.2. Oscillatory pumping tests

Oscillatory pumping tests and the associated monitoring of pressure changes represent the fundamental method used for characterization of sandbox properties before, during, and after NAPL infiltration. To implement an oscillatory pumping test, a variable-speed electric motor connected to a small piston was used, which alternately injected and extracted water at a pumping port (see Zhou et al., 2016 for further details). To collect baseline data, we performed oscillatory pumping tests prior to introducing NAPL into the aquifer, using the 5 pumping locations indicated in Fig. 1. Similar to Zhou et al. (2016), at each location we performed oscillatory pumping tests at periods of 2, 5, 10, and 20 s and recorded corresponding head change observations at all 10 observation locations. As discussed in Cardiff et al. (2013), this use of multiple periods for aquifer characterization is expected to yield additional information about hydraulic properties relative to testing at a single period. For each test, the piston used had a total volume of 4 ml, meaning that a total of 4 ml of fluid is oscillated into and out of the sandbox per

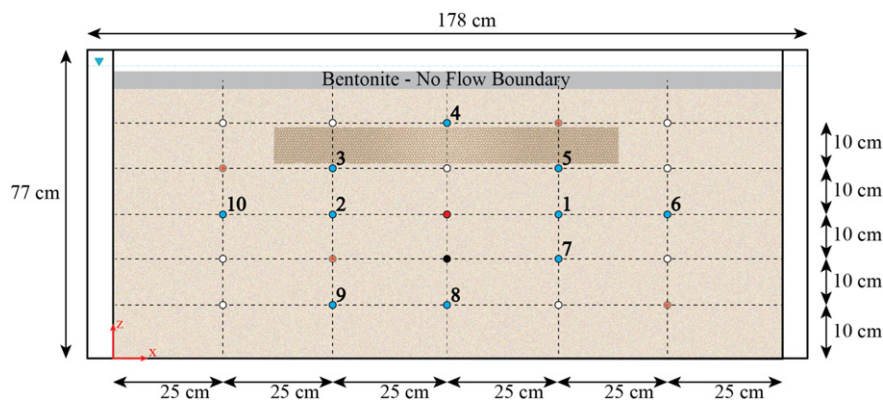


**Fig. 1.** 2-D diagram of sandbox construction, with darker regions representing a lower-conductivity layer. Blue points represent observation locations, red represent available pumping locations, and black represents NAPL injection location. White points represent unused ports.

oscillation period. Pressure changes at all monitoring points were observed, and generally after 5–6 periods of pumping the responses at all observation points obtained so-called “steady-periodic” conditions, in which the amplitude and phase of head change signals at each location were consistent. The steady-periodic condition was determined by observing the stabilization of all head measurements through the data collection software on a computer (see, e.g. Fig. 2).

During and after NAPL injection, oscillatory pumping tests were performed daily, using only the central pumping location in the sandbox, and associated pressure changes were recorded at the surrounding 10 observation locations. The same pumping periods and volumes were used as described above, and oscillatory pumping was again performed until steady-periodic conditions were achieved visually.

### 2.3. NAPL injection

In our experiments, to avoid toxicity concerns the infiltrating NAPL used is simple vegetable oil, with density of  $0.91 \text{ g/cm}^3$  and viscosity of 40–80 cP. The vegetable oil was dyed with a blue organic dye (Kingscote Chemicals, Inc.) to enable visualization. In creating the NAPL “source zone”, 3 liters of the vegetable oil was injected at a rate of 50 ml/min over 60 min. The NAPL was injected at a port approximately 25 cm above the bottom boundary in the center of the aquifer (black marker, Fig. 1) using 1/8" tubing attached to a peristaltic pump.

After injection, the dyed NAPL was observed to circularly spread outward from the injection location. Over a period of several days, the NAPL gradually moved upward and eventually ponded below the low conductivity silt layer. Based on visual and photographic observations throughout time, we found most of the NAPL appeared to collect below the silt layer and ceased moving once the silt layer was encountered. A small amount of NAPL was left as residual phase near the injection point where the sand appears dyed. Local heterogeneity due to

packing appears to have caused some additional lateral spreading of NAPL resulting in a wider zone of contamination than expected. Overall, the observation of NAPL spill is fairly similar to that documented by Illman et al. (2010), though the use of an LNAPL (vegetable oil) rather than a DNAPL (TCE) reverses the direction of the buoyancy that the contaminant experiences. In addition, during the NAPL migration we regularly took time-lapse photos of the sandbox to visually image spreading throughout time (Fig. 3). Following completion of the experiment we visually verified (during sandbox excavation) that NAPL infiltration was consistent across the thickness of the sandbox, in order to verify that the flow could be treated as effectively two-dimensional.

Regarding the NAPL used in these experiments, vegetable oil has a relatively higher contrast in kinematic viscosity (when compared to water) than is seen in many chlorinated solvent contaminants, such as TCE or PCE. However, many LNAPLs including varieties of fuel oil and coal tar display properties similar to that of the vegetable oil used (see Table 1).

Likewise, while not completely representative of a realistic contaminated site, we note that the experimental design is meant to mimic the arrangement of pumping and observation wells that may be available surrounding a NAPL source zone. For example, the central pumping well is located above the source zone, representing the direction in which contaminant movement is expected due to buoyancy. In contaminated sites, pumping wells are likely to similarly be placed down-gradient of estimated source zones in order to capture dissolved plumes. The arrangement of observation wells is also similar to what may be seen at contaminated sites. For example, only one well is located up-gradient of the contaminated area (bottom of the sandbox), while a range of wells are placed down-gradient and at the edges of the plume. This arrangement is consistent with the plan-view arrangement of wells that might be seen many field sites, where “bounding” wells are used to locate the lateral and transverse extent of a plume. That said, a true NAPL-

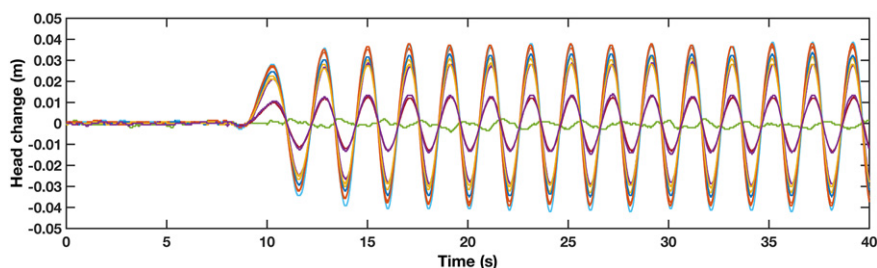


**Fig. 2.** Raw head change data collected during one oscillatory pumping test. Nominal pumping period of 2 s was used in this case, with pumping beginning roughly 8 s after start of record. Steady periodic conditions are obtained at approximately 20 s.



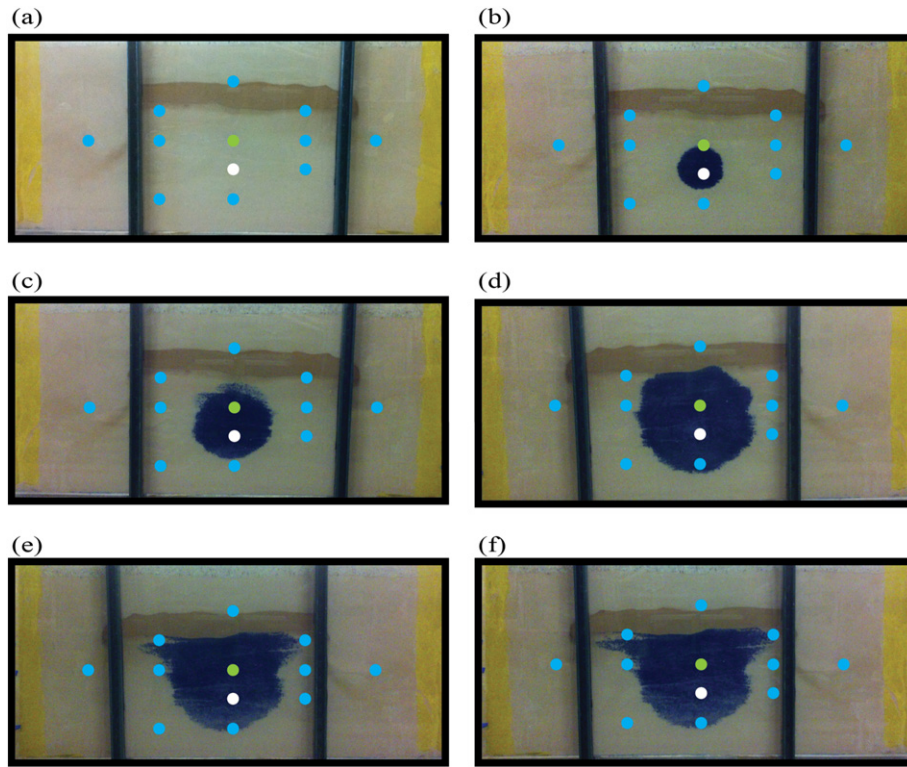


**Fig. 3.** Sandbox aquifer (a) before NAPL injection; (b) during NAPL injection; (c) At completion of NAPL injection; (d) 5 days after NAPL injection; (e) 10 days after NAPL injection; (f) 15 days after NAPL injection.

contaminated site would present significantly greater difficulties due to both observational limitations and the three-dimensional character of realistic contamination.

## 2.4. Data analysis strategy

### 2.4.1. Data processing

At the end of each oscillatory pumping test, a time series of pressure data from all monitoring locations has been collected, represented in terms of head change from the pre-test state. Before further analysis, the beginning of each time series is first trimmed to remove the non-steady-periodic section of response, during which amplitudes and phases of head response are varying. Ten periods worth of steady-periodic data are then selected from the testing results for further processing. The trimmed time-series data was then processed spectrally; Fourier coefficients that contain phase and amplitude information were extracted through signal analysis, as described in Zhou et al. (2016). The Fourier coefficients associated with the dominant frequency in the spectra are then extracted, referred to henceforth as the phasor data. This phasor data consists of two coefficients per observation location that minimize the misfit to the observed, trimmed data:

$$\min_{A_{obs,j}, B_{obs,j}} \sum_k (h_j(t_k) - A_{obs,j} \cos(\omega t_k) + B_{obs,j} \sin(\omega t_k))^2 \quad (2)$$

**Table 1**

Kinematic viscosities of selected NAPL groundwater contaminants.

Fluid	Kinematic viscosity (cSt, $1 \times 10^{-6} [\text{m}^2/\text{s}]$ )
Water (20 °C)	1
TCE	0.39
PCE	0.54
coal tar	~30–100
Fuel oils	~30–700
Vegetable oil	~44–88

where  $h_j(t_k)$  represents the trimmed time-series head change data at time  $t_k$ ,  $\omega [T^{-1}]$  represents the angular frequency of the dominant (pumping) period, and  $A_{obs,j}$  and  $B_{obs,j}$  represent sinusoidal and cosinusoidal coefficients to be optimized. We note here that though pumping periods of 2, 5, 10, and 20 s were targeted, the electric piston pump was manually set each time. Thus, the pumping periods deviated somewhat from these ideal values and were estimated as part of data processing. In the following sections, the phasor coefficients are represented equivalently as a complex number  $\Phi_{obs,j} = A_{obs,j} + iB_{obs,j}$ . By applying Euler's formula, the best-fitting phasor is equivalently:

$$\min_{\Phi_{obs,j}} (h_j(t_k) - \text{Re}[\Phi_{obs,j} \exp(i\omega t_k)])^2 \quad (3)$$

This processed phasor data, which stores information about the amplitude and phase shift of signals at the known dominant (stimulation) frequency, was then used as the input for inverse modeling.

### 2.4.2. Forward model

In the case of an aquifer saturated with water, experiencing Darcian flow conditions and forced at a single frequency, the groundwater flow equations can be represented in the frequency domain as:

$$\begin{aligned} i\omega S_s(\mathbf{x})\Phi_h &= \nabla \cdot (K(\mathbf{x})\nabla\Phi_h) + \Phi_q \quad \forall \mathbf{x} \in \Omega \\ \Phi_h &= 0 \quad \forall \mathbf{x} \in \Gamma_d \\ \nabla\Phi_h \cdot \mathbf{n} &= 0 \quad \forall \mathbf{x} \in \Gamma_n \end{aligned} \quad (4)$$

This is an extended form based on Cardiff et al. (2013), where  $\Omega$  is the domain of interest;  $\mathbf{x}[L]$  is a vector of spatial coordinates;  $\Gamma_d$  and  $\Gamma_n$  represent Dirichlet (no head change) and Neumann (no flow) boundaries, respectively;  $\omega [T^{-1}]$  is the angular frequency of oscillation;  $S_s(\mathbf{x}) [L^{-1}]$  is a scalar field of specific storage;  $K(\mathbf{x}) [LT^{-1}]$  is a scalar field of hydraulic conductivity values (assumed isotropic), and  $\mathbf{n}$  represents the outward normal to a boundary. The quantities  $\Phi_q$  and  $\Phi_h$  are complex field variables representing the phasors of the forcing

(pumping) and head change (response), i.e.:

$$\begin{aligned} h(\mathbf{x}, t) &= \text{Re}[\Phi_h(\mathbf{x}) \exp(i\omega t)] \\ q(\mathbf{x}, t) &= \text{Re}[\Phi_q(\mathbf{x}) \exp(i\omega t)] \end{aligned} \quad (5)$$

where  $h(\mathbf{x}, t)[L]$  represents head changes due to the oscillatory forcing and  $q(\mathbf{x}, t)[T^{-1}]$  represents volumetric sources of water per unit volume of aquifer. The formulation (4) applies when steady-periodic conditions have been reached within an aquifer, such that the amplitude and phase of head changes are consistent with time (see, e.g., Cardiff et al., 2013).

A key benefit of the frequency-domain formulation (4) is that it is effectively steady-state and can thus be solved quickly, without numerical time-stepping. In addition, it should be noted that steady-periodic heads inherently depend on both  $K$  and  $S_s$  meaning that both of these parameters may be estimated as part of inversion. To simulate the above equations numerically, we use a finite volume flow model developed in MATLAB, which can solve for steady-periodic responses within the aquifer, after initial transient response has dissipated. An open source version of this code has recently been made available in Cardiff et al. (2016 (in review)). In the particular model used here, the sandbox was discretized into 1800 cells with each cell of  $0.025 \text{ m} \times 0.025 \text{ m} \times 0.1 \text{ m}$ . The top boundary and bottom are no flow boundaries while the left and right boundaries are treated as constant head conditions, to represent the laboratory conditions.

At the short timescales over which oscillatory pumping occurs, we consider both the aquifer material and the distribution of fluids to be roughly static. Similarly, because of the short periods and small oscillation volumes used, the impact of oscillatory pumping on fluid distributions was assumed to be minimal (and was observed to be so during experiment visualization). Thus, when NAPL infiltration occurs, we assumed that the same steady-periodic governing equations could be utilized, but that an effective change in local conductivity and storage parameters occurs, i.e.:

$$i\omega(S_s(\mathbf{x}) + \Delta S_s(\mathbf{x}))\Phi_h = \nabla \cdot ((K(\mathbf{x}) + \Delta K(\mathbf{x}))\nabla\Phi_h) + \Phi_q \quad \forall \mathbf{x} \in \Omega \quad (6)$$

in which  $\Delta S_s(\mathbf{x})$  and  $\Delta K(\mathbf{x})$  represent the changes in local effective specific storage and hydraulic conductivity, respectively, due to the change in fluid saturations at that local aquifer volume.

#### 2.4.3. Inversion approach

To estimate properties within the sandbox (that is,  $K(\mathbf{x})$  and  $S_s(\mathbf{x})$ ), and their effective changes with time, we utilize an inversion (tomography) algorithm. After processing of head data, the input data for tomography consists of the head change phasors measured across all observation locations, pumping locations, and frequencies. The forward model described above is then used to simulate these same observations when a given pattern of  $K$  and  $S_s$  heterogeneity is defined in the numerical model. During inverse modeling, the discretized  $K$  and  $S_s$  values within the numerical model are updated until an appropriate fit between observed and simulated observations is obtained.

During inversion, we utilize the quasi-linear geostatistical algorithm developed by Kitanidis (1995), in which the following objective function is minimized:

$$\min_{\mathbf{s}, \beta} \frac{1}{2} (\mathbf{y} - \mathbf{h}(\mathbf{s}))^T \mathbf{R}^{-1} (\mathbf{y} - \mathbf{h}(\mathbf{s})) + \frac{1}{2} (\mathbf{s} - \mathbf{X}\beta)^T \mathbf{Q}^{-1} (\mathbf{s} - \mathbf{X}\beta) \quad (7)$$

where, given  $m$  measurements and  $n$  parameters,  $\mathbf{s}$  is the  $(n \times 1)$  vector of parameter values;  $\mathbf{y}$  is the  $(m \times 1)$  vector of data (an organized list of real and imaginary parts of the head phasor measured from each location, frequency, and pumping location);  $\mathbf{h}(\cdot)$  is the physical forward model described above, which takes as input parameter values and outputs expected observations;  $\mathbf{R}$  is the  $(m \times m)$  covariance matrix of data errors for the head phasor measurements;  $\mathbf{X}$  is a  $(n \times p)$  vector of drift functions,  $\beta$  is a  $(p \times 1)$  vector of drift coefficients; and  $\mathbf{Q}$  is the  $(n \times n)$  prior parameter covariance. In performing minimization, the objective

function above is linearized and the corresponding linear optimization problem is repeatedly solved until convergence (for further details see, e.g., Cardiff et al., 2012).

This inversion algorithm is used in two different contexts. In the case where no existing estimates of aquifer heterogeneity are available, spatially-distributed  $\ln(K)$  and  $\ln(S_s)$  constitute the unknown vector  $\mathbf{s}$ , which we refer to as “background imaging”. Similarly, though, the forward model may be populated with estimated  $K$  and  $S_s$  values based on background imaging, and the geostatistical approach may then be applied in order to estimate spatially distributed  $\Delta \ln(K)$  and  $\Delta \ln(S_s)$  values, representing differential changes from this background – we refer to this as “differential imaging”.

### 3. Results

In this section, data processing and imaging analysis results are discussed. First, we discuss the results of data processing to extract steady-periodic signal characteristics at all monitoring locations. Though the complex phasor and its real and imaginary coefficients were used in the actual inversion routines, here we present signal characteristics in terms of their relative amplitude and phase delay. Relative amplitude refers to the amplitude of the recorded signal normalized by the amplitude of the head signal at the pumping well; phase delay represents the delay in seconds of the recorded signal relative to considering the pumping well head signal as “zero” phase delay. These metrics, discussed in Section 3.1, are easily translated into phasor coefficients, though we believe amplitude and phase are more intuitive for simple visualization.

After discussing the results of signal processing, which provide a qualitative sense of oscillatory pumping tests’ sensitivity to heterogeneity and fluid movements, we present inversion results for both background imaging and several rounds of differential imaging in Section 3.2. Here, we first assess a “best case” scenario in which aquifer heterogeneity has been well-characterized before NAPL infiltration. We then present a more realistic scenario in which aquifer characterization begins after NAPL infiltration has already begun.

#### 3.1. Signal processing results

The sensitivity of oscillatory pumping test signals to heterogeneity in  $K$  and  $S_s$  can be seen at first pass by simply plotting the obtained observations spatially. During NAPL infiltration, as well, phase and amplitude changes are visible which can be qualitatively informative without the need for detailed inverse modeling. Based on a known input frequency of stimulation (i.e., as determined by the pumping period), we extracted Fourier coefficients of the signal at this given frequency from the raw pressure data. These Fourier coefficients can then be presented more intuitively as amplitude and phase measures of the pressure responses. In Fig. 4, normalized amplitudes and phase maps are shown before and during NAPL infiltration for the case of pumping at the central sandbox location at a period of 5 s. Of particular note, amplitudes are substantially lower across all locations following the completion of NAPL injection, decreasing by approximately a factor of 25 throughout. Similarly, phase delays increase for all locations initially, indicating an increase of “travel time” through the NAPL fluid. Similar trends in amplitudes and phase changes are observed for 2, 10 and 20- s period testing, indicating a low effective  $K$  zone developing below the silt layer. At later times (e.g., Fig. 4g,h), sensors located below the NAPL plume show slight increases in amplitude and decreases in phase, possibly suggesting a movement of the main NAPL plume upward and away from these sensors (though residual NAPL is seen left behind).

The results of signal processing show that the contrast in effective properties caused by vegetable oil clearly impact signal amplitude and phase. It is likely that even more subtle contrasts in fluid properties would be recognizable given this strong sensitivity.

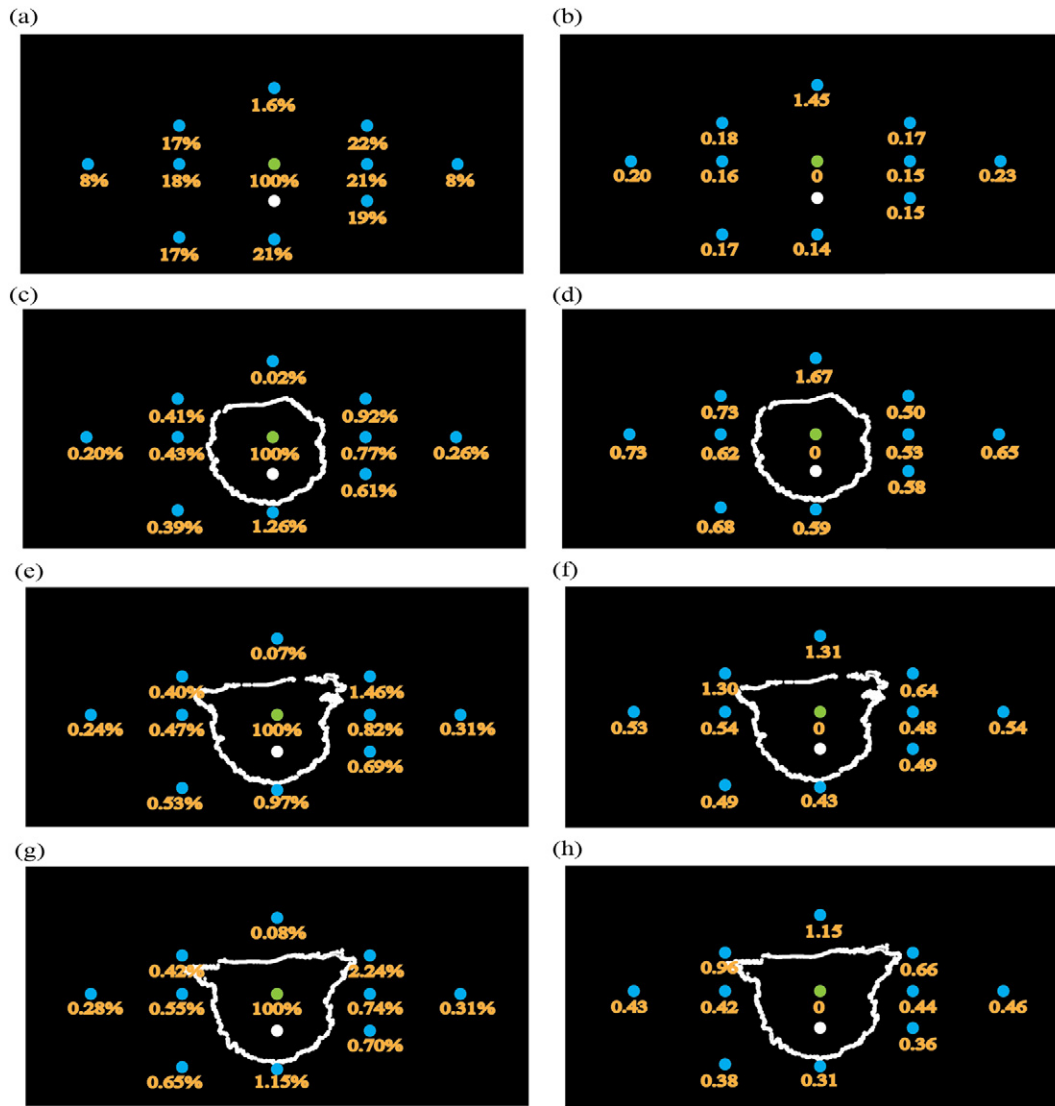


**Fig. 4.** Amplitude (left column) and phase delay in seconds (right column) for testing at 5 s period. Rows represent results of testing (a, b) before NAPL injection, (c, d) 1 day after NAPL injection, (e, f) 5 days after NAPL injection, and (g, h) 15 days after NAPL injection. White outlines represent approximate location of NAPL plume as assessed through image processing.

### 3.2. Tomography (imaging) results

Tomography was applied to the head phasor datasets using the Bayesian geostatistical algorithm described above. In applying the geostatistical algorithm for background tomography, we assumed that  $\ln(K)$  and  $\ln(S_s)$  were uncorrelated random fields with the same underlying correlation scales ( $\lambda_x = 0.7$  m,  $\lambda_y = 0.1$  m). In the case of this work, these parameters were based on the known heterogeneity within the sandbox. However, in realistic field applications, these parameters would have to be estimated based on presumed subsurface heterogeneity (e.g., through studying of outcrops). Given the relatively lower ranges in  $S_s$  variability relative to  $K$  variability, we assumed variances of  $\sigma_{\ln(K)}^2 = 1.3$  and  $\sigma_{\ln(S_s)}^2 = 0.2$ . These variances and correlation scales represent values that are similar to the statistics of the actual heterogeneity in aquifer sediments. The first  $m/2$  parameters of the vector  $\mathbf{s}$  represented  $\ln(K)$  values, with the second  $m/2$  parameters of the vector representing  $\ln(S_s)$  values. The matrix  $\mathbf{Q}$  thus had the form:

$$\mathbf{Q} = \begin{bmatrix} \text{cov}(\ln(K)) & 0 \\ 0 & \text{cov}(\ln(S_s)) \end{bmatrix}$$

where  $\text{cov}(\ln(K))$  and  $\text{cov}(\ln(S_s))$  are matrices defined by the spatial covariance of  $\ln(K)$  and  $\ln(S_s)$ , respectively. Similarly, the matrix  $\mathbf{X}$

represented that  $\ln(K)$  and  $\ln(S_s)$  fields were assumed to have spatially constant, unknown means, i.e.:

$$\mathbf{X} = \begin{bmatrix} 1 & 0 \\ \vdots & \vdots \\ 1 & 0 \\ 0 & 1 \\ \vdots & \vdots \\ 0 & 1 \end{bmatrix}$$

During differential imaging, we utilized correlation lengths of  $\lambda_x = 0.5$  m and  $\lambda_y = 0.2$  m, which was based on the rough dimensions of the NAPL plume after initial injection. Again, in realistic field applications, the correlation lengths of the NAPL plume would have to be estimated by other methods, such as stochastic numerical analog experiments, which could assess likely geostatistical parameters for plume extent within the given geologic environment. Alternately, correlation lengths may be estimated through Bayesian procedures such as the Restricted Maximum Likelihood estimator (Kitanidis, 1995).

Inversion was carried out iteratively using linearization of the objective function formulas (7), with convergence declared once the following two conditions were met: 1) There was a relative change in the total objective function of less than 0.01%; and 2) There was a maximum



relative change of 0.1% in any parameter value estimated between iterations. These convergence criteria were small enough that no discernable change in imaging results were present at the completion of the algorithm. All inverse modeling runs were executed using a MacBook Pro with 2.6 GHz Intel Core i7 processor and 16GB of RAM. Individual forward model runs generally required a few seconds a few seconds, while convergence of the numerical inversion generally required roughly 20 iterations and completed within roughly 10 min of wall-clock time.

The first set of imaging results, presented in Fig. 5, show a case in which detailed characterization information is available before the NAPL “spill”. In this case, we utilized the Bayesian geostatistical algorithm to estimate  $\ln(K)$  and  $\ln(S_s)$  based on data from pumping at all five possible locations, at periods of 2, 5, 10, and 20 s, and observed at all 10 monitoring locations, resulting in a total of 400 inverted observations (note that two Fourier coefficients, or analogously the signal amplitude and phase, are inverted). These background imaging results (Fig. 5a,b) are able to clearly delineate the heterogeneity (silt layer) near the top of the sandbox, which appears as an area of low hydraulic conductivity and high specific storage. Using this background imaging results as the assumed  $K$  and  $S_s$  values, we then inverted data collected during NAPL infiltration and estimated values of  $\Delta \ln(K)$  and  $\Delta \ln(S_s)$ , which utilized data only from pumping tests performed at the central pumping location. As before, observations of head phasors at all observation locations were inverted, across pumping periods of 2, 5, 10, and 20 s, for a total of 80 inverted observations. The imaging results produced show the estimates of these changes from data collected immediately following NAPL injection (Fig. 5c,d), five days after NAPL injection (Fig. 5e,f), and 15 days after NAPL injection (Fig. 5g,h). To give a better visual comparison between the lab-observed NAPL migration and computed  $K$  imaging results, we have placed the plume contours at different

times (obtained via simple image processing to extract blue areas from the associated photographs) on top of the corresponding  $K$  imaging results. Overall, the differential imaging appears to capture the upward movement of the plume over time, seen primarily as a low- $K$  region, though the tomography appears to result in significant “smearing” of the obtained image relative to the visually observed plume (see white outlines in Fig. 5). Similarly, there are other regions within the imaging results that experience both increased and decreased  $K$  estimates outside of the plume extent, which are likely artifacts of the inversion and the relatively limited data. In all cases described above, the observed data in phasor form were compared to those produced from model simulation, similar to the work presented in Zhou et al. (2016), and the two data sets achieved very high agreement, with roughly 2% misfit ( $\text{RMSE} \approx 0.001$  m) across all inversions (Fig. 6).

The idealized case above assumes that useful information is available about aquifer structure before contamination. However, this is likely not realistic for many aquifer contamination scenarios, in which focused characterization only ends up being performed after a source of contamination has already been detected. In real field investigations of detecting subsurface contaminant sources such as NAPL, it is common then that one does not know the subsurface heterogeneity (e.g.  $K$  and  $S_s$  distributions) with much certainty. To represent this more common case, we again performed baseline and differential imaging. However, in this set of analyses the baseline imaging was performed after the NAPL injection had been completed (thus representing a combination of both inherent aquifer heterogeneity and fluid property contrasts), and using only the pumping tests performed at the central pumping well. The background imaging results from this case is shown in Fig. 7a,b, where we note that lower- $K$  regions are found both at the location of the aquifer’s silt layer, as well as surrounding the point of NAPL injection. Differential imaging was then performed for the data collected

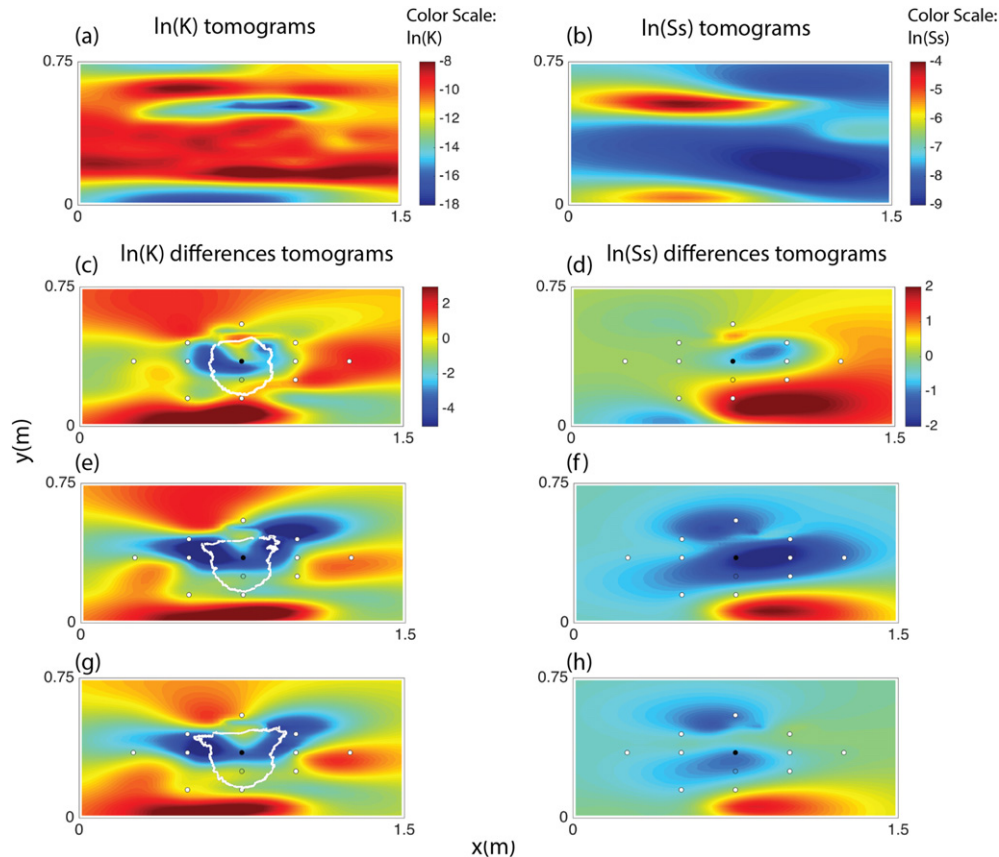


**Fig. 5.** Tomography results under idealized scenario. Background tomogram (a, b) utilizes data from all 5 pumping tests. Differential tomograms (c–h) utilize only data from central pumping location, and represent results for 1 day after NAPL injection, 5 days after NAPL injection, and 15 days after NAPL injection.

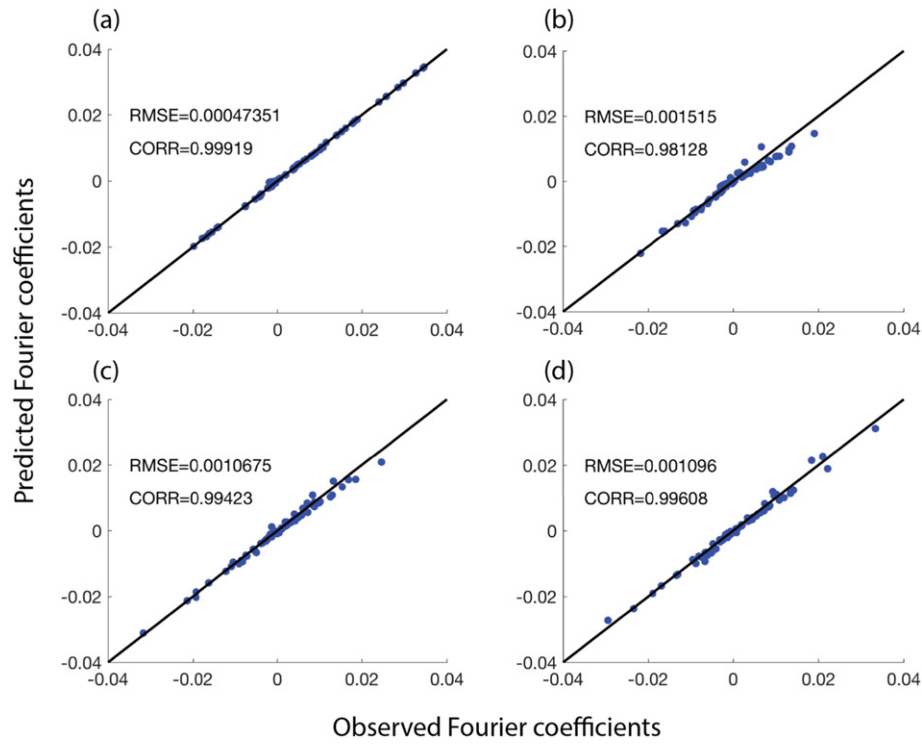


**Fig. 6.** Cross-plots of data fit for background imaging case. Points represent all phasor coefficients across all pumping locations and testing periods. Results from inversion of data from (a) uncontaminated sandbox, (b) 1 day after NAPL injection (c) 5 days after NAPL injection, and (d) 15 days after NAPL injection.

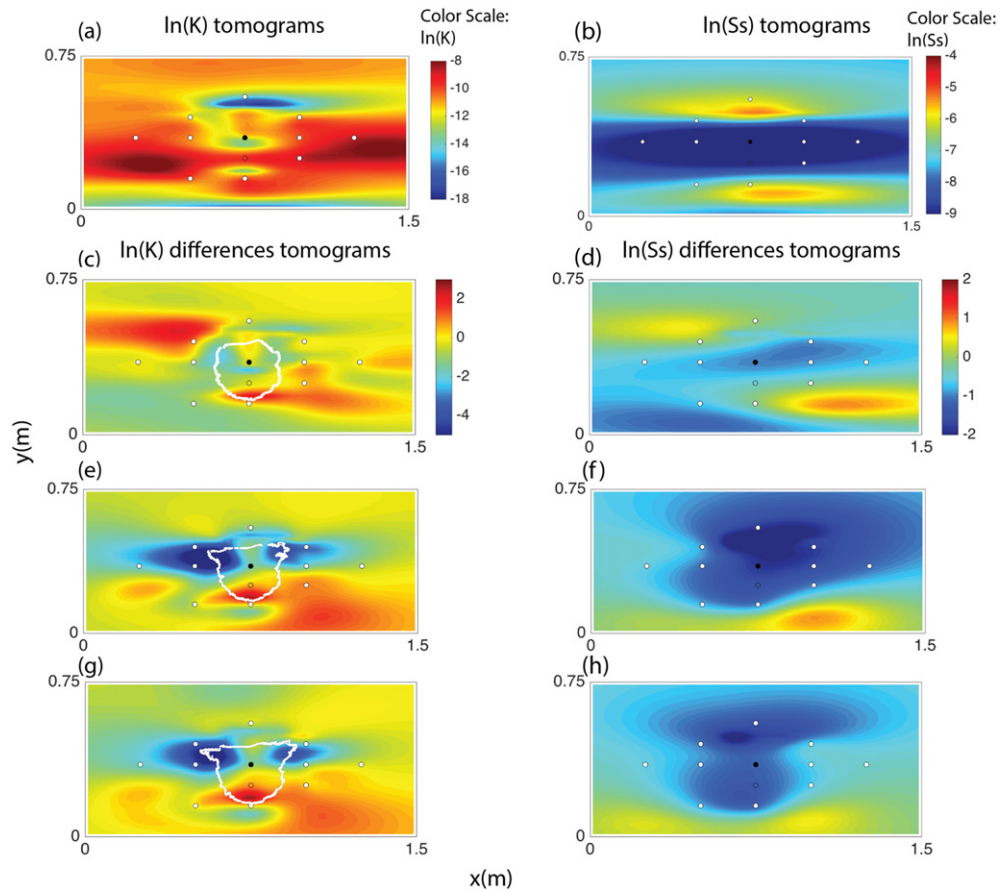


**Fig. 7.** Tomography results under more realistic imaging scenario. Background imaging results (a, b) utilizes data only from pumping at central location, after injection of NAPL was completed. Differential imaging results (c–h) represent changes in effective parameters from background values at 1, 5 and 15 days following injection, again using only data from pumping at the central pumping port.



1 day, 5 days and 15 days after the NAPL “spill”, again using only data from pumping tests performed at the central well. In these cases (Fig. 7c–h), the key regions of  $\Delta \ln(K)$  and  $\Delta \ln(S_s)$  observed are: 1) Decreases in  $\ln(K)$  located directly below the location of the silt layer, indicating trapping and pooling of the low-viscosity NAPL fluid below this layer; and 2) Increases in  $\ln(K)$  below the injection port, indicating upward movement of the plume and a loss of low-viscosity fluid below the injection port, again due to buoyant movement.

We note in this second case that it would be impossible to differentiate, based on the background imaging, between low-conductivity geologic layers and interpreted low-conductivity layers that are, in fact, due to high-viscosity fluid infiltration. Thus, the background imaging in this second case is of less practical use. However, the observation of changes in effective  $K$  heterogeneity with time are only possible if dynamic processes alter the effective  $K$  of a region over time. In this case, the changes in effective  $K$  are associated with the upward movement of the buoyant, low-viscosity fluid. However, similar techniques may be applied in cases where precipitation, biofilm growth, or other processes may interact to jointly change effective  $K$  within portions of an aquifer.

In all cases, we note that estimates of  $\Delta \ln(S_s)$  show less coherence and lower overall magnitudes, generally indicating that respective changes in  $S_s$  are less than one order of magnitude. There are several reasons why  $S_s$  changes appear to be more difficult to image in practice. For one, compressibilities of common fluids including water and oil generally fall within a narrow range of less than one order of magnitude, meaning that fluid invasion will not produce a substantial contrast in the effective specific storage. Secondly, the sensitivity of hydraulic tomography data to  $S_s$  variations is generally lower than to  $K$  variations, making contrasts in this property more difficult to detect.

### 3.3. Comparisons via a numerical experiment

The imaging results presented above appear to show that NAPL saturation can be imaged using the proposed OHT techniques, though the

resolution of features through differential imaging is qualitatively somewhat low. Several choices and issues in tomography problems can impact this resolution, including the information content of the observations (i.e., their sensitivity to imaged properties), the number and location of observations, the accuracy of the forward model utilized (in terms of accurately representing system physics), the degree of noise present in the data, and the choices of regularization parameters used (in this case, geostatistical correlation lengths chosen).

Some of these effects are best studied through numerical experiments, in which the degree of noise can be controlled and the impact of imperfect forward modeling assumptions can be eliminated. Here we present a set of numerical experiments in which background and differential imaging were performed similarly to the sandbox inverse modeling described above. True parameter fields representing the period before NAPL injection, during injection, and after plume development are shown in Fig. 8. In each case, the silt used in the sandbox was assumed to have lower  $K$  and higher  $S_s$  relative to the surrounding sand, and the NAPL plume was presumed to affect local effective parameter values by lowering  $K$  by a factor of 10. Data were generated by simulating the same pumping tests described for the laboratory setup, and random data noise comparable to ~10% of the average observed signal was added to these synthetic data.

The results of background imaging and differential imaging are shown in Fig. 9 for the “ideal” case in which 5 pumping tests were available to characterize the aquifer pre-NAPL infiltration for baseline characterization, and 1 pumping test was used to characterized differential changes to the sandbox effective  $K$  values during NAPL infiltration. Overall, we note a high degree of similarity to the actual laboratory sandbox results, with the position of the plume captured although smoothed due to the limited data availability and the impacts of regularization. Similarly,  $S_s$  values obtained are less reliable, showing variability during differential imaging even though this parameter is not at all affected by the synthetic plume infiltration. The causes of this relict variability appears to be errors in the initial imaging of  $S_s$  values during

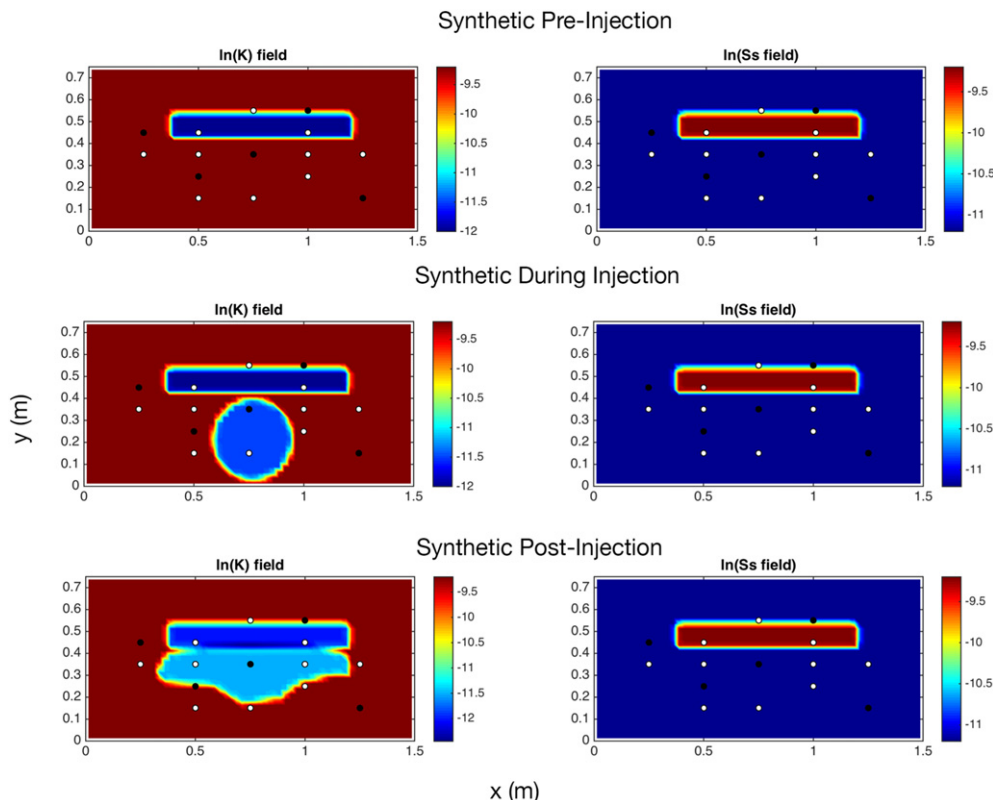
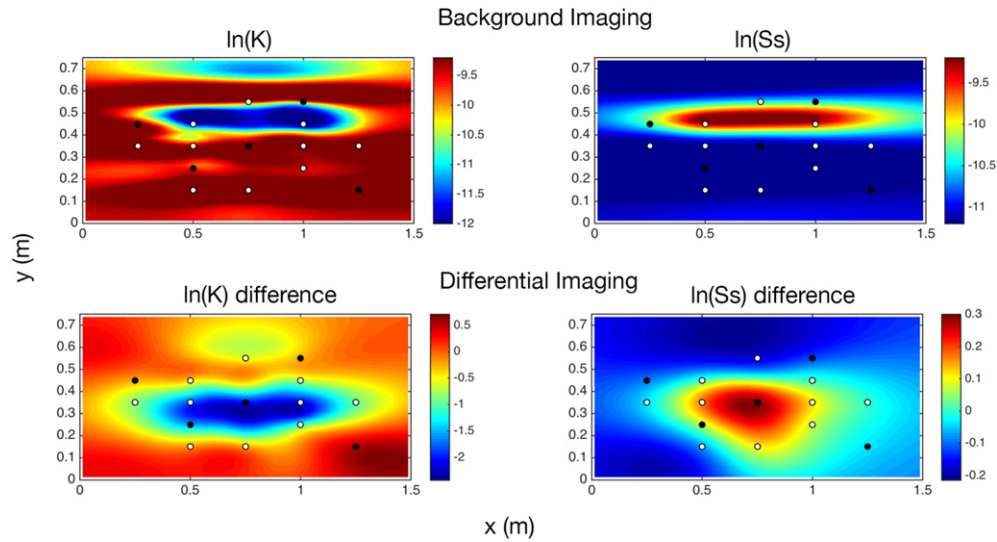


Fig. 8. Synthetic  $\ln(K)$  and  $\ln(S_s)$  fields used to test OHT background imaging and differential imaging.



**Fig. 9.** Background and differential imaging for the “ideal” case, in which 5 pumping tests are used to perform background imaging characterizing properties before NAPL injection (Fig. 8, top). Differential imaging uses a single pumping test to characterize changes post-injection (Fig. 8, bottom).

background imaging, which then impact differential imaging results. Overall, we also note that OHT imaging of Ss is somewhat less reliable than K imaging, which is expected given the relative sensitivity of HT to these two parameters and the overall smaller range of Ss variability seen in natural systems.

Similarly, we have performed a numerical experiment similar to the “more realistic” imaging case, in which the initial background imaging takes place using a single pumping test after the NAPL has been injected, and differential imaging is performed after the NAPL plume has evolved and moved upwards toward the clay layer. The similarities to the sandbox imaging results are striking. In the case of the background imaging (Fig. 10, top), which takes place during initial infiltration of the NAPL plume, the plume itself is imperfectly imaged, likely due to the limited data availability (only a single pumping location). The pattern of K values imaged (Fig. 10, top) is quite similar to that seen in Fig. 7a, and Ss values are relatively poorly recovered. During differential imaging (Fig. 10, bottom), the numerical experiment shows increases in effective K toward the bottom of the sandbox (from which the NAPL has moved out of), and decreases in effective K beneath the clay layer, as the NAPL

spreads at this location. This is remarkably similar to what is seen in the actual sandbox results (compare with Fig. 7e, g). Ss values are more poorly recovered, and show changes during differential imaging even though Ss is not changing; again, this appears to be due to the errors in initial imaging of Ss values, which are then propagated in differential imaging.

Overall, the numerical experiments appear to support the following conclusions: 1) The results obtained by treating the NAPL plume as a change to “effective” K within the sandbox are quite similar to what is obtained if K values are changed in numerical experiments; this suggests that the effective K approximation to modeling multi-phase systems as roughly steady under OHT pumping is valid; 2) Errors in imaging of both background K and differential K are likely due to the relatively small number of pumping tests performed on the sandbox and the incomplete coverage of observations; and 3) Errors in imaging of background K and Ss values can be propagated during differential imaging. With regards to the second point, the sandbox experiments created were designed to represent realistic field-scale sites, where incomplete coverage and sparse testing density are often a reality. A more dense

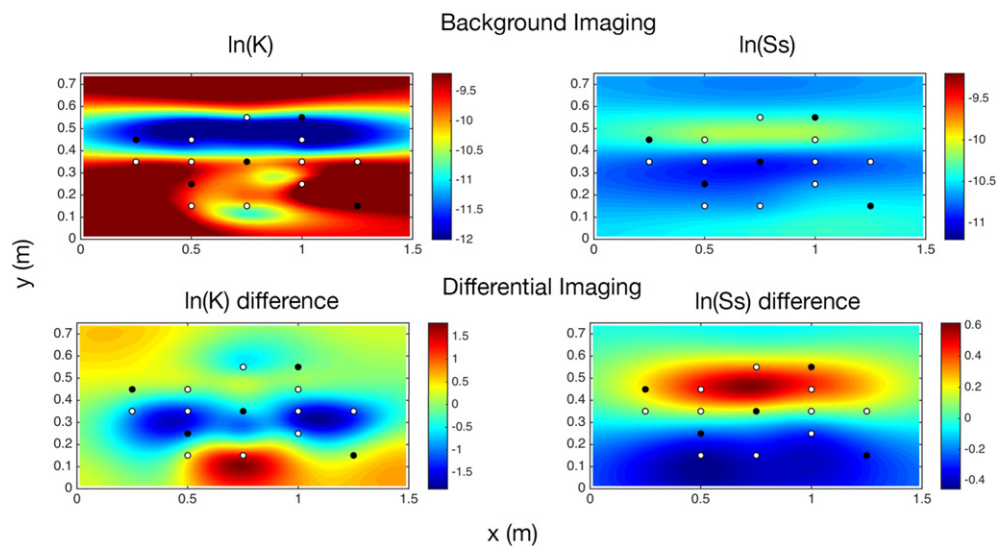


**Fig. 10.** Background and differential imaging for the more “realistic” case, in which 1 pumping test is used to perform background imaging characterizing properties during NAPL injection (Fig. 8, center). Differential imaging uses a single pumping test to characterize changes at post-injection stage (Fig. 8, bottom).

testing and observational network would doubtlessly improve imaging results, but perhaps would be unrealistic in real field application and have the effect of “over-selling” lab-scale results.

#### 4. Discussion and conclusions

Oscillatory hydraulic tomography represents a strategy for long-term characterization that could be applied with little impact at many contaminated sites. An oscillating pressure signal can be generated within an aquifer either through a dedicated injection/extraction system, or by superimposing sinusoidal flowrate changes at an existing pumping well. In either case, the strategy will have minimal impact on the distribution of contaminants and on regional hydraulic gradients (in contrast to traditionally suggested approaches for applying hydraulic tomography). The main design parameters that must be defined for such testing are the frequency/period of the stimulations and the magnitude of stimulation necessary to obtain a reliable signal (for guidelines, see Cardiff and Barrash, 2015). In this work, the effectiveness of using oscillatory hydraulic tomography (OHT) for characterizing aquifer heterogeneity was further investigated for its use in differential imaging. Through laboratory experiments, we have shown that repeated OHT testing could provide a useful strategy for NAPL source zone monitoring, and that effective  $K$  changes within some portion of the aquifer of roughly one order of magnitude – which can be caused by changes in fluid properties, biofouling, or other processes – would be easily distinguished. In an ideal scenario, this change in effective  $K$  could be translated into an understanding of changes in NAPL saturation within a contaminated volume. However, in practice other effects, such as a change in interfacial surface area and phase boundary geometry, biofilm growth, or other effects may also lead to changes in effective  $K$  within an aquifer volume. The combination of information from OHT with other geophysical methods, such as electrical resistivity or induced polarization measurements, or with information may help to address this issue of non-unique reasons for  $K$  changes.

Other approaches that have been tested for understanding NAPL saturation, such as the use of partitioning tracer tests (see, e.g., similar proof-of-concept work in Illman et al., 2010) would provide complementary, and likely highly beneficial information to OHT tests. A key benefit that should be noted, however, is that OHT is mass conservative (no net injection or extraction), and can be performed over relatively short timeframes, with useful pumping periods generally in the range of seconds to hours (see, e.g., Cardiff and Barrash, 2015). The use of multiple partitioning tracer tests in NAPL source zones is likely to require both longer timeframes and greater care in the treatment and disposal of extracted fluids during testing.

As with many tomography approaches, it should also be noted that the results of imaging will be highly dependent on the distribution of sources and receivers (i.e., pumping and monitoring wells). However, OHT appears to be able to produce differential imaging results that are consistent with observed processes at the scales investigated. When applied in concert with other methods, such as geophysical characterization, OHT may provide a complementary data source that can directly detect changes to the effective hydraulic properties within an aquifer volume and help to constrain site models.

Overall, through laboratory experiments and numerical modeling, OHT shows promise as a minimally-invasive approach for characterizing NAPL source zones and for differential imaging of effective hydraulic properties. For potential field applications, it appears that one can perform site characterization with relatively few pumping and observation locations, and without mass fluid extraction or injection.

#### References

Annable, M.D., Rao, P., Hatfield, K., Graham, W.D., Wood, A., Enfield, C., 1998. Partitioning tracers for measuring residual NAPL: field-scale test results. *J. Environ. Eng.* 124 (6): 498–503. [http://dx.doi.org/10.1061/\(ASCE\)0733-9372\(1998\)124:6\(498\)](http://dx.doi.org/10.1061/(ASCE)0733-9372(1998)124:6(498)).

- Babcock, E., Bradford, J.H., 2015. Reflection waveform inversion of ground-penetrating radar data for characterizing thin and ultrathin layers of nonaqueous phase liquid contaminants in stratified media. *Geophysics* 80 (2), H1–H11.
- Bear, J., 1972. *Dynamics of Fluids in Porous Media*. Elsevier Publishing Co, New York.
- Brewster, M.L., Annan, A.P., Greenhouse, J.P., Kueper, B.H., Olhoeft, G.R., Redman, J.D., Sander, K.A., 1995. Observed migration of a controlled DNAPL release by geophysical methods. *Ground Water* 33 (6):977–987. <http://dx.doi.org/10.1111/j.1745-6584.1995.tb00043.x>.
- Cardiff, M., Barrash, W., 2011. 3-D transient hydraulic tomography in unconfined aquifers with fast drainage response. *Water Resour. Res.* 47, W12518. <http://dx.doi.org/10.1029/2010WR010367>.
- Cardiff, M., Bakhos, T., Kitanidis, P.K., Barrash, W., 2013. Aquifer heterogeneity characterization with oscillatory pumping: Sensitivity analysis and imaging potential. *Water Resour. Res.* 49 (9):5395–5410. <http://dx.doi.org/10.1002/wrcr.20356>.
- Cardiff, M., Barrash, W., 2015. Analytical and semi-analytical tools for the design of oscillatory pumping tests. *Ground Water* 53 (6):896–907. <http://dx.doi.org/10.1111/gwat.12308>.
- Cardiff, M., Barrash, W., Kitanidis, P.K., 2012. A field proof-of-concept of aquifer imaging using 3D transient hydraulic tomography with temporarily-emplaced equipment. *Water Resour. Res.* 48, W05531. <http://dx.doi.org/10.1029/2011WR011704>.
- Cardiff, M., Lim, D., Zhou, Y., 2016. OHT3DINV: An efficient 3-D code for oscillatory and steady-state hydraulic tomography applications. *Comput. Geosci.* (in review).
- Chambers, J.E., Wilkinson, P.B., Wealhall, G.P., Loke, M.H., Dearden, R., Wilson, R., Allen, D., Ogilvy, R.D., 2010. Hydrogeophysical imaging of deposit heterogeneity and groundwater chemistry changes during DNAPL source zone bioremediation. *J. Contam. Hydrol.* 118 (1), 43–61.
- Dietrich, P., Butler, J.J., Faiss, K., 2008. A Rapid Method for Hydraulic Profiling in Unconsolidated Formations. *Ground Water* 46 (2), 323–328.
- Dogan, M., Van Dam, R.L., Bohling, G.C., Butler, J.J., Hyndman, D.W., 2011. Hydrostratigraphic analysis of the MADE site with full-resolution GPR and direct-push hydraulic profiling. *Geophys. Res. Lett.* 38 (6).
- Dwarakanath, V., Deeds, N., Pope, G.A., 1999. Analysis of partitioning interwell tracer tests. *Environ. Sci. Technol.* 33 (21), 3829–3836.
- Gottlieb, J., Dietrich, P., 1995. Identification of the permeability distribution in soil by hydraulic tomography. *Inverse Probl.* 11, 353–360.
- Halihan, T., Paxton, S., Graham, I., Fenstemaker, T., Riley, M., 2005. Post-remediation evaluation of a LNAPL site using electrical resistivity imaging. *J. Environ. Monit.* 7 (4), 283–287.
- Hochstetler, D.L., Barrash, W., Leven, C., Cardiff, M., Chidichimo, F., Kitanidis, P.K., 2015. Hydraulic tomography: continuity and discontinuity of high-K and low-K zones. *Groundwater* 54 (2):171–185. <http://dx.doi.org/10.1111/gwat.12344>.
- Illman, W.A., Berg, S.J., Liu, X., Massi, A., 2010. Hydraulic/partitioning tracer tomography for DNAPL source zone characterization: small-scale sandbox experiments. *Environ. Sci. Technol.* 44 (22):8609–8614. <http://dx.doi.org/10.1021/es101654j>.
- Jin, M., Delshad, M., Dwarakanath, V., McKinney, D.C., Pope, G.A., Sepehrnoori, K., Tilburg, C.E., Jackson, R.E., 1995. Partitioning tracer test for detection, estimation, and remediation performance assessment of subsurface nonaqueous phase liquids. *Water Resour. Res.* 31 (5), 1201–1211.
- Kitanidis, P.K., 1995. Quasi-linear geostatistical theory for inversing. *Water Resour. Res.* 31 (10), 2411–2419.
- Kueper, B.H., Redman, D., Starr, R.C., Reitsma, S., Mah, M., 1993. A field experiment to study the behavior of tetrachloroethylene below the water table: spatial distribution of residual and pooled DNAPL. *Groundwater* 31 (5):756–766. <http://dx.doi.org/10.1111/j.1745-6584.1993.tb00848.x>.
- Liu, G., Butler, J.J., Bohling, G.C., Reboulet, E., Knobbe, S., Hyndman, D.W., 2009. A new method for high-resolution characterization of hydraulic conductivity. *Water Resour. Res.* 45 (8).
- Mayer, A., Hassanizadeh, S.M., 2005. *Soil and Groundwater Contamination: Nonaqueous Phase Liquids - Principles and Observations*. American Geophysical Union.
- Orozco, A.F., Kemna, A., Oberdörster, C., Zschornack, L., Leven, C., Dietrich, P., Weiss, H., 2012. Delineation of subsurface hydrocarbon contamination at a former hydrogenation plant using spectral induced polarization imaging. *J. Contam. Hydrol.* 136, 131–144.
- Parker, B., Cherry, J., Chapman, S., Guilbeault, M., 2003. Review and analysis of chlorinated solvent dense nonaqueous phase liquid distributions in five sandy aquifers. *Vadose Zone J.* 2 (2), 116–137.
- Parker, B.L., Chapman, S.W., Guilbeault, M.A., 2008. Plume persistence caused by back diffusion from thin clay layers in a sand aquifer following TCE source-zone hydraulic isolation. *J. Contam. Hydrol.* 102 (1–2):86–104. <http://dx.doi.org/10.1016/j.jconhyd.2008.07.003>.
- Parker, B.L., Cherry, J.A., Chapman, S.W., 2004. Field study of TCE diffusion profiles below DNAPL to assess aquitard integrity. *J. Contam. Hydrol.* 74 (1–4):197–230. <http://dx.doi.org/10.1016/j.jconhyd.2004.02.011>.
- Rao, P.S.C., Annable, M.D., Kim, H., 2000. NAPL source zone characterization and remediation technology performance assessment: recent developments and applications of tracer techniques. *J. Contam. Hydrol.* 45, 63–78.
- Revil, A., Schmütz, M., Batzle, M.L., 2011. Influence of oil wettability upon spectral induced polarization of oil-bearing sands. *Geophysics* 76 (5), A31–A36.
- Siegrist, R.L., Lowe, K.S., Crimi, M.L., Urynowicz, M.A., 2006. Quantifying PCE and TCE in DNAPL source zones: effects of sampling methods used for intact cores at varied contaminant levels and media temperatures. *Groundw. Monit. Remediat.* 26 (2): 114–124. <http://dx.doi.org/10.1111/j.1745-6592.2006.00085.x>.
- Yeh, J.T.-C., Liu, S., 2000. Hydraulic tomography: development of a new aquifer test method. *Water Resour. Res.* 36 (8), 2095–2105.
- Yeh, T.-C.J., Zhu, J., 2007. Hydraulic/partitioning tracer tomography for characterization of dense nonaqueous phase liquid source zones. *Water Resour. Res.* 43, W06435. <http://dx.doi.org/10.1029/2006WR004877>.
- Zhou, Y., Lim, D., Cupola, F., Cardiff, M., 2016. Aquifer imaging with pressure waves - evaluation of low-impact characterization through a sandbox study. *Water Resour. Res.* <http://dx.doi.org/10.1002/2015WR017751>.